### nature electronics

**Article** 

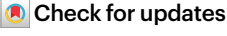
https://doi.org/10.1038/s41928-024-01196-y

## A self-filtering liquid acoustic sensor for voice recognition

Received: 5 September 2023

Accepted: 31 May 2024

Published online: 23 September 2024



Xun Zhao 13, Yihao Zhou<sup>1,3</sup>, Aaron Li 15, Jing Xu 15, Shreesh Karjagi<sup>1</sup>, Edward Hahm<sup>1</sup>, Lara Rulloda<sup>1</sup>, Justin Li<sup>1</sup>, John Hollister ©<sup>2</sup>, Pirouz Kavehpour<sup>1,2</sup> & Jun Chen **©**¹⊠

Wearable acoustic sensors can be used for voice recognition. However, the capabilities of such devices, which are typically based on solid materials, are often restricted by ambient noise, motion artefacts and low conformability to the skin. Here we report a liquid acoustic sensor for voice recognition. The approach is based on a three-dimensional oriented and ramified magnetic network structure of neodymium-iron-boron magnetic nanoparticles suspended in a carrier fluid, which behaves like a permanent magnet. The sensor can discriminate small pressures (0.9 Pa), has a high signal-to-noise ratio (69.1 dB) and provides self-filtering capabilities that can remove low-frequency biomechanical motion artefact (less than 30 Hz). We use the liquid acoustic sensor—together with a machine learning algorithm to create a wearable voice recognition system that offers a recognition accuracy of 99% in a noisy environment.

Voice is a potentially powerful basis for sophisticated human-machine interactions<sup>1-4</sup>. Wearable acoustic sensors can be directly attached to the throat to capture vocal cord vibrations<sup>5-7</sup>. However, wearable acoustic sensors for voice recognition are typically composed of solid materials such as piezoelectric materials<sup>8,9</sup>, polymer thin films<sup>10</sup>, metals<sup>11</sup> and two-dimensional materials<sup>12</sup>. These sensors rely on material deformation or vibration induced by sound pressure<sup>13,14</sup>, and their capabilities—and wider applications—are restricted due to poor skin conformability, limited sensitivity, narrow pressure detection range and instability against motion artefacts 15,16.

In this Article, we report a self-filtering liquid acoustic sensor for voice recognition and human-machine communication. The liquid acoustic sensor is based on a reconfigurable magnetic liquid-termed a permanent fluidic magnet (PFM)—that has a high remanent magnetization. The magnet is created by using non-Brownian neodymium-ironboron (NdFeB) magnetic particles to construct a three-dimensional (3D) oriented and ramified magnetic (ORM) network structure within a carrier fluid. The sensor has a storage modulus of 100-1,000 Pas (approximately three orders of magnitude lower than its solid counterparts) and eliminates non-conformal acoustic coupling, exhibiting an acoustic impedance of 1.61 MRayl (around 11 times lower than the acoustic impedance of solid sensors, which is 40 MRayl). The tunable rheological properties of the liquid sensor provide in-sensor noise filtering by selectively dampening mechanical noise below 30 Hz.

The sensors can discriminate pressures of 0.9 Pa and offer a signal-to-noise ratio (SNR) of 69.1 dB. They also have a frequency detection resolution of 0.01 Hz and a wide frequency response range from 30 Hz to 10 kHz. We use this sensor—together with a machine learning algorithm—to create a wearable voice recognition system that offers an accuracy of 99% in a noisy environment. We also show that the system can be used to control a wheelchair via voice commands.

#### **PFM**

Traditional acoustic sensors made of solid materials possess an acoustic impedance of around 40 MRayl, which is ten times higher than that of the biological tissues<sup>17</sup> (Fig. 1a). Solid materials cannot form a conformal interface with the curved surface of skin owing to their mechanical hardness (Supplementary Fig. 1). Currently, flexible sensors made of ultrathin elastomers exhibit improved contact with biological tissues<sup>18</sup> (Fig. 1b). However, mechanical mismatches and air gaps still exist, which can contribute to the increased acoustic impedance mismatches and limited acoustic sensing performance. This work addressed this central challenge by developing a liquid acoustic sensor as a new platform technology that gains better conformability and sensing performance

Department of Bioengineering, University of California, Los Angeles, Los Angeles, CA, USA. Department of Mechanical and Aerospace Engineering, University of California, Los Angeles, Los Angeles, CA, USA. <sup>3</sup>These authors contributed equally: Xun Zhao, Yihao Zhou. 🖂 e-mail: jun.chen@ucla.edu

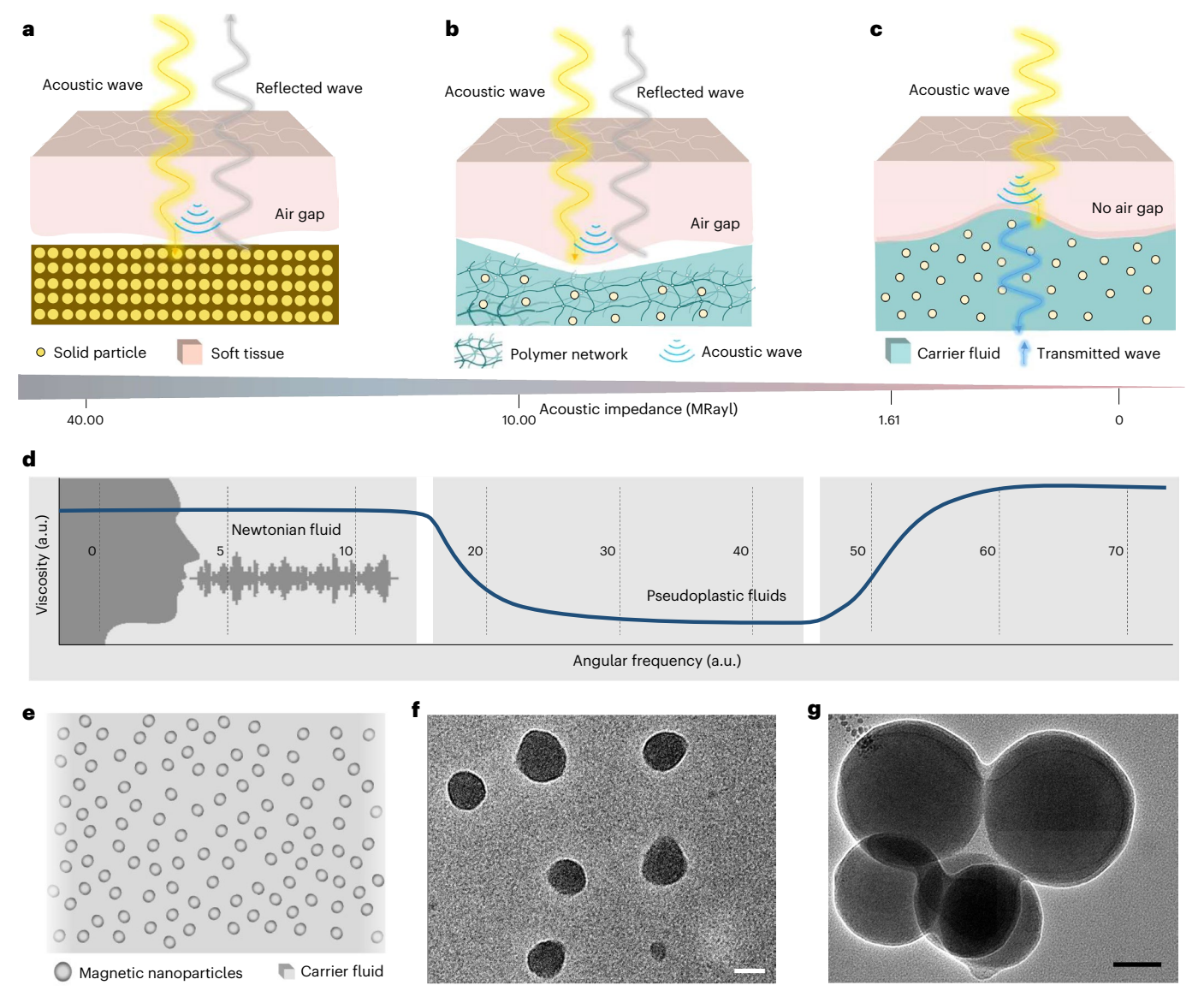
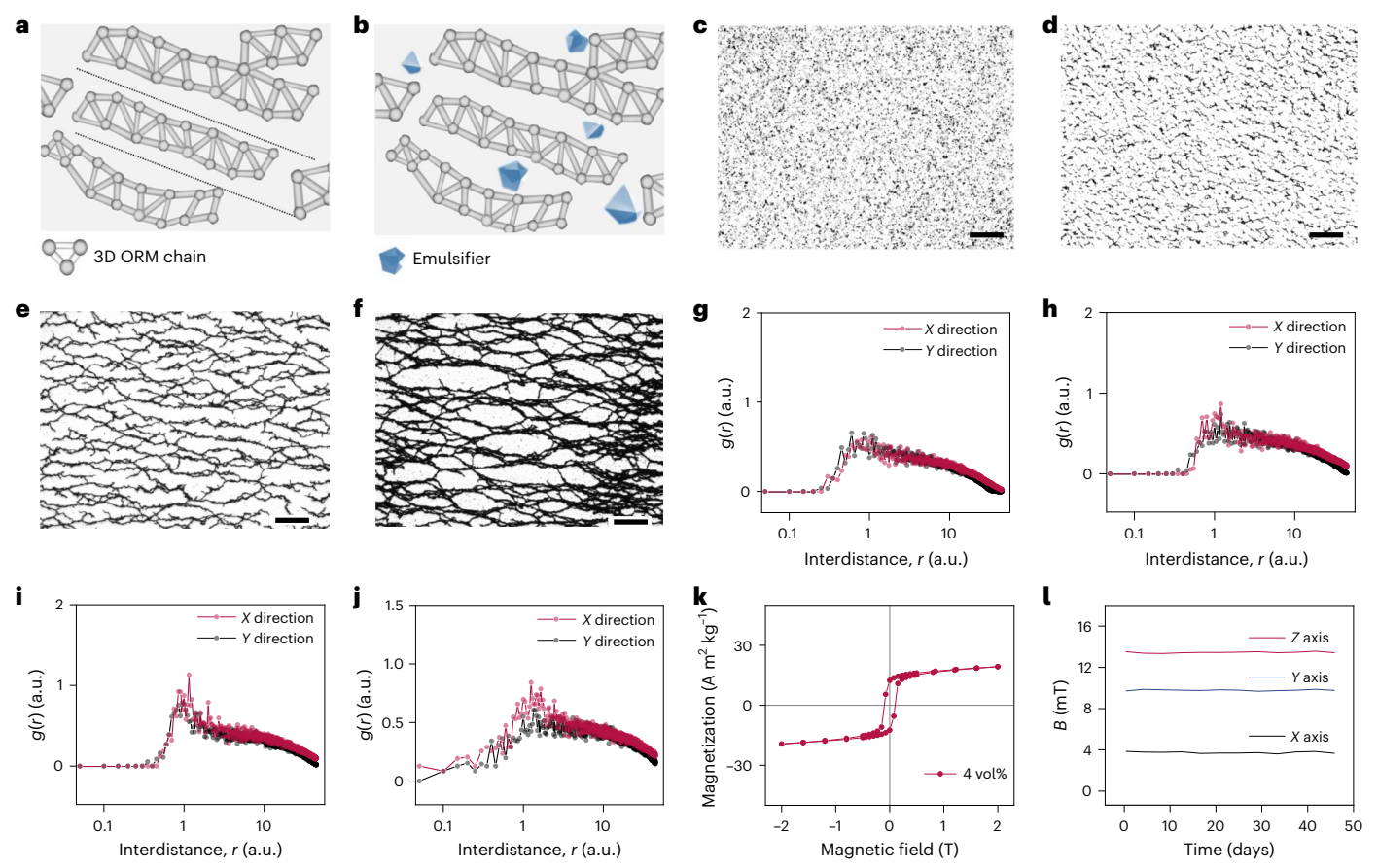


Fig. 1 | A self-filtering liquid acoustic sensor. a, Schematic of a conventional solid acoustic sensor that demonstrates the highest acoustic impedance with soft tissue. b, Schematic of a soft solid acoustic sensor that demonstrates relatively high acoustic impedance with soft tissue. c, Schematic of a liquid acoustic sensor that demonstrates the lowest acoustic impedance with soft

tissue.  ${f d}$ , Schematic showing the viscosity of the colloidal dispersion against angular frequency.  ${f e}$ , Magnetic nanoparticles dispersed in carrier fluids.  ${f f}$ , Transmission electron microscopy image of magnetic nanoparticles. Scale bar, 200 nm.  ${f g}$ , Transmission electron microscopy image of magnetic nanoparticles showing a coated nanolayer of SiO $_2$ . Scale bar, 60 nm.

than conventional solid counterparts. Using liquid materials to design an acoustic sensor would lower the acoustic impedance mismatches between the human body and the device, minimize reflections and promote the transmission of acoustic waves (Fig. 1c). The liquid acoustic sensor was built on PFM as the liquid material, with low mechanical hardness contributing to a conformal sensor-tissue interface and minimized impedance mismatches. Conventionally, liquid materials can be classified into three categories based on their rheological properties. Newtonian fluids exhibit a linear shear stress in response to external shear rate, yielding a consistent viscosity across various frequencies (Fig. 1d). Pseudoplastic fluids exhibit a decreasing viscosity with increasing shear rate, which responds better to low-frequency signals<sup>19,20</sup>. Conversely, dilatant fluids exhibit an increased viscosity in response to increasing shear rate, which allows them to respond better to high-frequency signals such as acoustic voice. Thus, among the three kinds of liquid material, we aim to design a fluid that is sensitive to voice signals and minimizes the low-frequency biomechanical motion artefacts from the human body (Supplementary Fig. 2).

Based on the design principles, we use PFM as a dilatant fluid inside. The magnetic nanoparticles form a 3D ORM network structure in the carrier fluid, which is distinct from the solid wavy chains within the polymer matrix<sup>21</sup>. Ferrofluids<sup>22</sup>-magnetic colloids-are paramagnetic and lose magnetization once the external magnetic field is removed. Maintaining ferromagnetism in a liquid state is challenging<sup>22,23</sup>. PFM can simultaneously maintain ferromagnetism and stability because of the 3D ORM network. To synthesize, we first uniformly immersed the NdFeB magnetic nanoparticles into the carrier fluids. We use ultrasonication to prevent particle aggregation and evenly disperse the nanoparticles in a state of equilibrium (Fig. 1e). NdFeB nanoparticles were uniformly dispersed within the carrier fluids, exhibiting an average diameter of 200 nm (Fig. 1f and Supplementary Fig. 3). To enhance their biocompatibility, we performed additional surface modifications through a SiO<sub>2</sub> layer coating (Fig. 1g). Subsequently, a pulse magnetic field was applied to the magnetic colloids, resulting in the formation of the 3D ORM network within the carrier fluid (Fig. 2a and Supplementary Figs. 4-6). The 3D network structure was also filmed (Supplementary Video 1).



**Fig. 2** | **Formation process of PFMs. a**, Magnetic nanoparticles organized in the flow adopt a head-to-tail configuration as the shear stress rate increases, where energy will be dissipated. The dotted line indicates the shear direction. **b**, Magnetic nanoparticle chain structure was restrained by clusters in higher shear stress. The energy is stored during deformation. **c**-**f**, Microscope images of the cross-section ORM network structure under a magnetic field of  $0.1\,\mathrm{T}(\mathbf{c})$ ,  $0.2\,\mathrm{T}(\mathbf{d})$ ,  $0.5\,\mathrm{T}(\mathbf{e})$  and  $1.5\,\mathrm{T}(\mathbf{f})$ . Scale bars,  $100\,\mu\mathrm{m}$ .  $\mathbf{g}$ - $\mathbf{j}$ , Direction-dependent pair

correlation function to characterize the ORM magnetic network. Calculation of the pair correlation function giving the g(r) value along the X and Y axes under a magnetic field of  $0.1\,\mathrm{T}$  ( $\mathbf{g}$ ),  $0.2\,\mathrm{T}$  ( $\mathbf{h}$ ),  $0.5\,\mathrm{T}$  ( $\mathbf{i}$ ) and  $1.5\,\mathrm{T}$  ( $\mathbf{j}$ ).  $\mathbf{k}$ , Relationship between remanent magnetization and the applied impulse magnetization.  $\mathbf{l}$ , Three-axis magnetic flux density of  $4.0\,\mathrm{vol}\%$  PFM over  $45\,\mathrm{days}$ , showing a negligible loss of magnetic strength.

The PFM was modified using diethylene glycol (DEG) to enable tunable rheological properties and to improve responsiveness to high-rate frequency signals (Fig. 2b). To understand the 3D ORM formation process, we captured microscope images under different magnetic field strengths. Under a magnetic field of 0.1 T, no evident orientation was observed (Fig. 2c). However, on increasing the magnetic field to 0.2 T, clusters began to form in the cross-section areas (Fig. 2d). With a further increase in the external magnetic field to 0.5 T, a greater degree of orientation became apparent. In particular, under a magnetic field of 1.5 T, the clusters grew and interconnected in branch-like patterns, forming a well-defined 3D ORM network structure (Fig. 2f and Supplementary Fig. 7). Consequently, as the magnetic field increases, the orientation of 3D ORM becomes more obvious. These findings provide valuable insights into the dynamic formation process and microstructural characteristics of the PFM. In addition, we use directional pair correlation function to analyse the degree of orientation. Initially, at low magnetic field levels, the statistical results showed that the particles exhibited a nearly equal possibility of orientation in the X and Y directions, indicating a lack of orientation (Fig. 2g). However, as the magnetic field increased, the probability of orientation in the X direction surpassed that in the Y direction (Fig. 2j). This is reflected in the increasing X/Y ratio, which rose from around 1.00 to 1.75. We also systematically examined the connectivity of the 3D ORM network structure using graph theory<sup>24</sup> to analyse the topological descriptor of average connected

nodes (Supplementary Fig. 8). We found that with the increase in magnetic field, the average connected nodes increased from 1.37 to 3.00 (Supplementary Fig. 9). As a result, the degree of magnetization will influence the orientation of the particles, with a clear preference for alignment in the  $\boldsymbol{X}$  direction as the magnetic field intensity increases. This finding matches with our Monte Carlo simulation (Supplementary Fig. 10).

The stable 3D ORM structure of the PFM is achieved through magnetic interactions among the nanoparticles. The PFM stability is achieved by the rigidity of the 3D network structure. This structure retains its magnetization even after the external magnetic field is removed, which was shown by 3D scanning imaging (Supplementary Fig. 11). From the magnetic hysteresis loop, the PFM demonstrated a coercivity of around 0.1 T and remanent magnetization of 12.4 A m<sup>2</sup> kg<sup>-1</sup> (Fig. 2k). Accordingly, we summarized the magnetic flux density of the PFM under varying impulse magnetic fields (Supplementary Fig. 12), revealing a linear relationship between them in the range of 0-1.89 T. In particular, the remanent magnetization saturates at 1.8 T. Beyond this threshold, further increase in the magnetic field did not yield any changes in the magnetic flux density of the PFM. To assess the long-term stability of the PFM, we measured the remanent magnetization in the absence of an external magnetic field over a period of 46 days using a three-axis Hall effect sensor. The PFM retained its remanent magnetizations in all the three directions (Fig. 21). These studies demonstrate the stability of the ferromagnetism of PFMs.

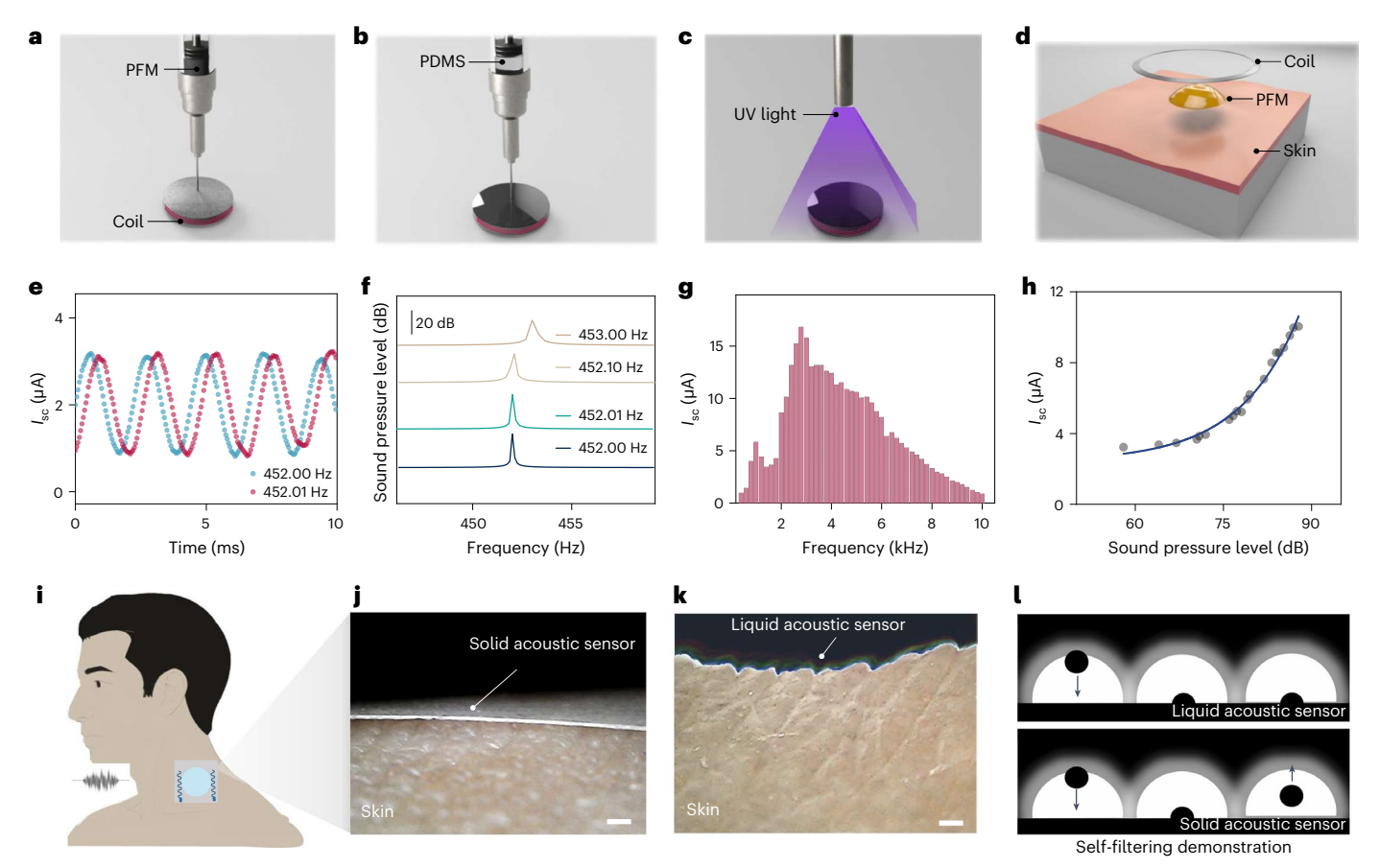


**Fig. 3** | **Fabrication of liquid acoustic sensors. a–d**, Schematic of the liquid acoustic sensor fabrication including permanent fluidic magnets injected into a copper coil (**a**), coating with a thin layer of PDMS (**b**), curing with UV light (**c**) and layering the fully constructed device on top of the skin (**d**). **e**, Output current of the liquid acoustic sensor under a frequency of 452.00-452.01 Hz and sound pressure level of 70 dB. **f**, FFT-processed frequency spectrum of a typical electrical output for frequencies of 453.00, 452.10, 452.01 and 452.00 Hz (from top to bottom). **g**, Frequency response measurement of the liquid acoustic sensor with a 4 vol% PFM. **h**, Effect of sound pressure level on the output current

amplitude. The blue line represents the fitted relationship between the sound pressure level and the output current amplitude. i, Liquid acoustic sensory system converts acoustic waves into mechanical vibrations and then into electrical signals by using a coil receiver. j, Solid-state acoustic sensor shows a poor interface with biological tissues. Scale bar, 250 µm. k, Liquid acoustic sensors can conformally attach to the throat for voice recognition. Scale bar, 250 µm. l, Schematic of solid and liquid devices demonstrate viscoelastic and damping properties verified by dropping a metal ball on the device.

#### PFM-based liquid acoustic sensors

Wearable acoustic sensors are typically made of solid materials, which play an important role in communications with the ability to augment human auditory perception by increasing situational acoustic awareness and promote the intelligibility of acoustic information. Solid sensors have low skin conformability, which leads to poor sensing performance<sup>5,25,26</sup>. PFM-based liquid acoustic sensors could improve the sensing performance (Fig. 3a). To form our sensor, we initially inject the PFM into a conductive coil structure. To prevent diffusion during subsequent applications, a thin layer of polydimethylsiloxane (PDMS) is coated on one side of the sensor surface (Fig. 3b) and then cured under ultraviolet (UV) light, resulting in the formation of a thin membrane on the surface (Fig. 3c). The other side of the device without the membrane can be securely attached to the skin in a conformal manner (Fig. 3d). When exposed to acoustic pressure, the PFM undergoes deformation in response to subtle throat vibrations, which converts sound pressure into magnetic field fluctuations. This is ascribed to the displacement of the PFM as a whole relative to the throat. Subsequently, the coil detects these magnetic field variations and generates electrical signals through magnetic induction according to Faraday's law. As a result, liquid acoustic sensors convert subtle sound pressure into high-fidelity electrical signals for acoustic sensing (Supplementary Note 1).

The designed liquid acoustic sensor achieves good skin conformability. First, since 450 Hz is a common frequency in human voice, varying frequencies ranging from 452 to 453 Hz were applied to the liquid acoustic sensor, and its detection resolution was measured. Figure 3e displays the typical electrical output for frequencies of 452.00 and 452.01 Hz, whereas Fig. 3f shows the corresponding frequency spectrum via fast Fourier transform (FFT). Our liquid acoustic sensor demonstrates a detection resolution of 0.01 Hz. We further tested the liquid acoustic sensor performance under sound waves over a frequency range from 0.4 to 10.0 kHz (Fig. 3g). The corresponding electrical output across the entire spectrum is shown in Supplementary Fig. 13 and we show a sensing range up to 10 kHz, which is larger than the frequency range of human voice. Our sensor can respond to a small pressure of 0.9 Pa (Supplementary Fig. 14). We further conducted measurements of the electrical output at various sound pressures. As the sound pressure increased from 55 to 90 dB, the observed current rose from 3.0 to 11.6  $\mu A$ (Fig. 3h). This behaviour can be attributed to the amplified vibration of  $the liquid \, a coustic \, sensor \, resulting \, from \, the \, increased \, sound \, pressure.$ 

#### Skin conformability and self-filtering capability

A key feature of the PFM is its conformable interface with the curved skin (Fig. 3i). Solid-material-based wearable acoustic sensors with high mechanical hardness exhibit poor conformability with the curved skin surface, which negatively impacts the acoustic sensing

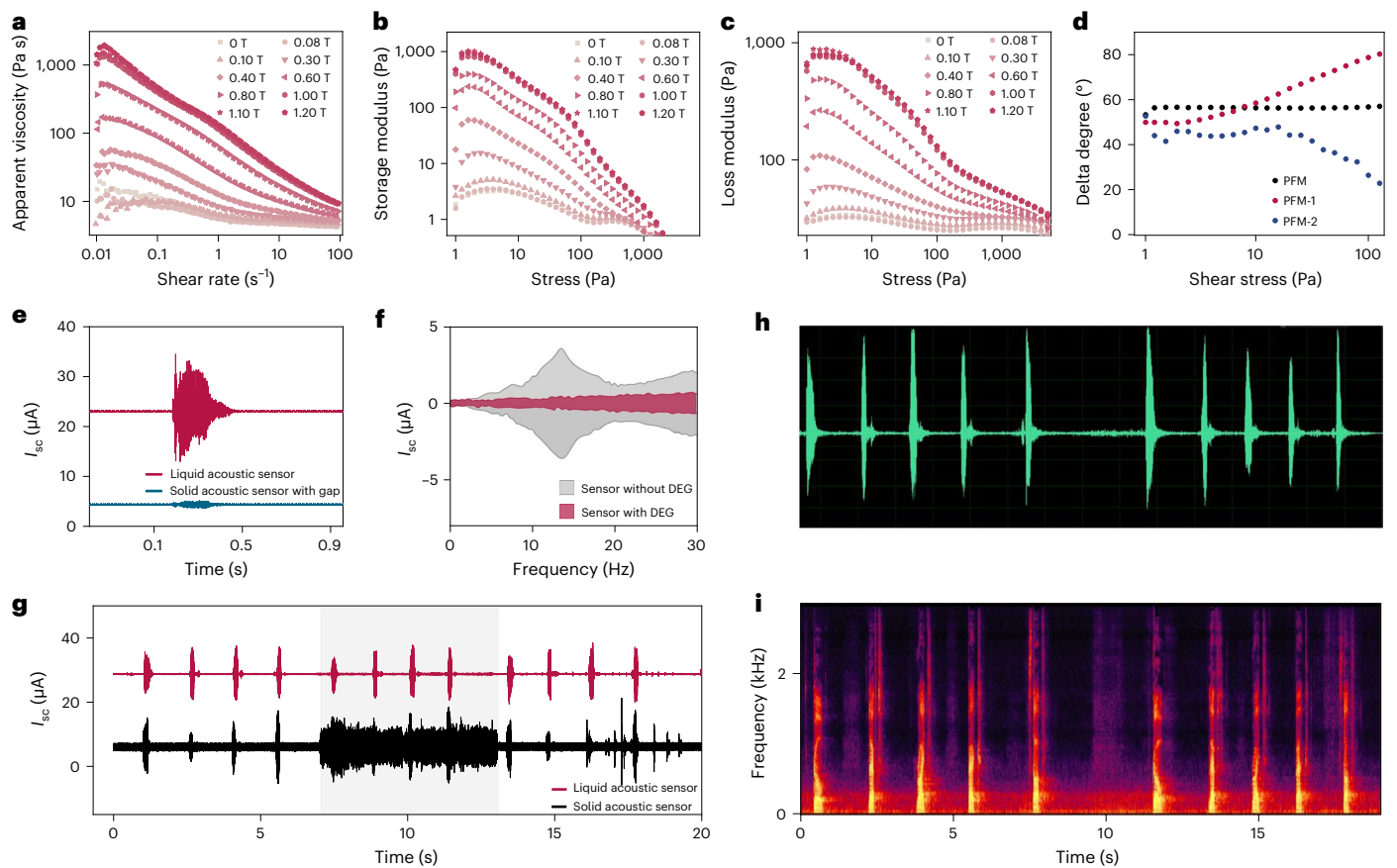


**Fig. 4** | **Characterization of liquid acoustic sensors. a**, Apparent viscosity of PFMs under different magnetic fields and at different shear rates. **b**, Storage modulus of 4.0 vol% PFM as a function of shear stress under different magnetic fields. **c**, Loss modulus of 4.0 vol% PFM as a function of shear stress under different magnetic fields. **d**, Delta degrees of PFMs with and without emulsifiers under different shear stresses: PFM, magnetic nanoparticles mixed with alginate as the carrier fluid; PFM-1, PFM mixed with polyethylene glycol; PFM-2, PFM mixed with DEG. **e**, Electrical output from the capacitive-based solid acoustic

sensor and our liquid acoustic sensor. **f**, Electrical signal of the liquid acoustic sensor containing DEG (red line), and the liquid acoustic sensor without DEG (grey line) showing in-sensor filtering characteristics. **g**, Comparison of output current signals of the liquid acoustic sensor and solid sensor for five voice commands. The shaded region represented both sensors in a simulated noise environment (90 dB). **h**, **i**, Acquired current signals (**h**) and the corresponding short-time Fourier transforms spectrograms (**i**).

performance  $^{5,27-31}$ . Even though solid materials can be fabricated in the form of a thin-film (around 20  $\mu$ m) structure, a noticeable sensor–skin interface gap still exists (Fig. 3j). In contrast, liquid-state materials offer a promising solution by providing a conformable sensor–skin interface, minimizing the occurrence of gaps and acoustic impedance mismatch (Fig. 3k and Supplementary Fig. 15). This is because liquid molecules have higher mobility and can freely slide and diffuse. When a liquid is applied to the skin's surface, its molecules can quickly rearrange to adapt to the skin's contours. This molecular mobility allows the liquid materials to closely adhere to the skin's surface, achieving optimal conformability. Additionally, our PFM has weaker intermolecular forces and lower surface tension and therefore can fill uneven surfaces of the skin.

The acoustic sensor has adjustable rheological properties. This enables the modification and optimization of its frequency detection range to naturally occurring human voice waves. Although digital filters can help mitigate noise, excluding epochs with artefacts will result in a loss of meaningful information<sup>32</sup>. However, the PFM-based liquid acoustic sensor allows for the extraction of clean sound pressure signals through the mitigation of low-frequency motion artefacts. The self-filtering property of the liquid acoustic sensor stems from the adaptable rheological properties of the PFM. In essence, the deformability of the ORM network, as well as the variation in macroscopic magnetic flux density, is frequency dependent and can be tuned by

shear thinning or shear thickening of the carrier fluids by adding different additives. This feature can be used to design liquid acoustic sensors capable of filtering out specific ranges of frequencies. The drop-ball test on the device demonstrates the elastic property of a conventional solid device and the fluidic property of the liquid acoustic sensor (Fig. 31 and Supplementary Video 2). Thus, to study the self-filtering property of the acoustic sensor, we conducted rheological tests on the PFM under different magnetization conditions.

Figure 4a illustrates the relationship between viscosity, magnetization and shear rate, showing an increasing trend of viscosity as the magnetic field intensifies from 0 to 1.2 T and a decreasing trend of viscosity as the shear rate increases from 0.01 to 100.00 s<sup>-1</sup>. This increase in viscosity with the magnetic field indicates that the PFM can utilize a reversible chain break-reconnection process inside the 3D ORM network structure within the carrier fluid to dissipate energy. The decrease in viscosity with shear rate indicates that the PFM exhibits a shear-thinning behaviour, which can be attributed to the increased chain breakage at high shear rates. Additionally, the storage and loss modulus values increased with an increase in magnetic field, which confirmed the formation of the 3D ORM network structure within the PFM. Both storage and loss modulus values decreased with an increase in shear rates, demonstrating the shear-thinning behaviour (Fig. 4b,c). We note that the measured storage modulus of the PFM is at the level of 100-1,000 Pa s, 100 times smaller than the conventional soft solid materials.

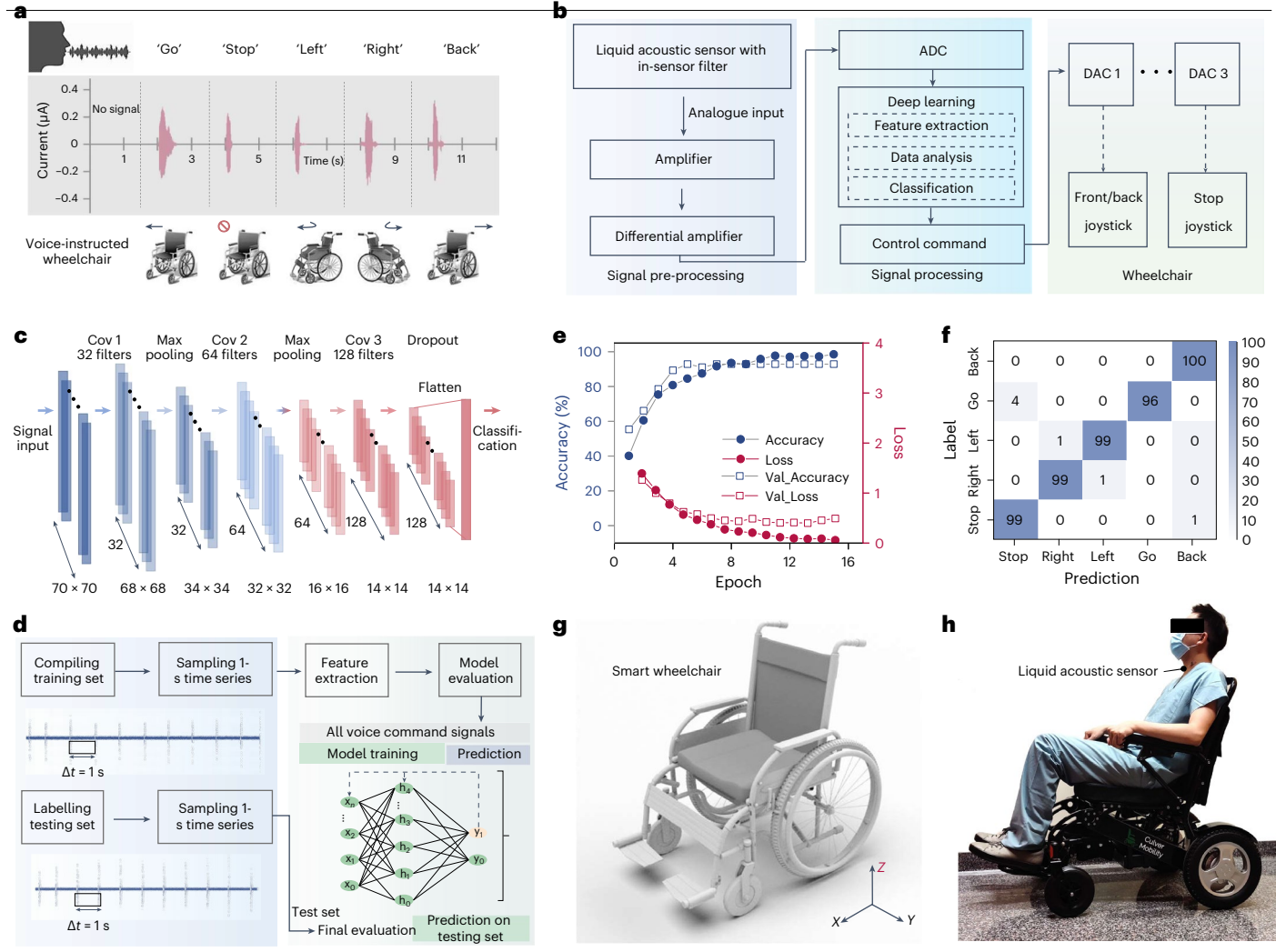


Fig. 5 | Wearable voice recognition system based on the liquid acoustic sensor. a, Output current signals of the liquid acoustic sensor for five voice commands: 'go', 'stop', 'left', 'right' and 'back'. b, Schematic showing three components on a customized printed circuit board. DAC, digital-to-analogue converter. c, Schematic of a three-layer CNN used in the voice recognition algorithm. d, Diagram showing the deep learning procedure. e, Evolution of the

model accuracy as well as loss function during the training epochs. Val-Accuracy shows the validation accuracy, and Val-Loss shows the validation loss. **f**, Confusion matrix of the recognition result. **g**, Schematic of the wheelchair. **h**, Picture showing the liquid acoustic sensor accurately capturing the commands, enabling the control of the wheelchair with voice.

When the PFM was modified by adding emulsifiers to the carrier fluids, a shear-thickening property was observed. The PFM exhibits a more pronounced viscoelastic behaviour with an increase in shear stress indicated by the delta degree (Fig. 4d). The additives tend to form temporary clusters, which, in turn, increase the flowing resistance and raise the viscosity of the fluid. These findings indicate that the rheological behaviour of the PFM can be modified by adjusting the magnetization and the additives. Given that noises emanating from human bodily activities typically fall within a low-frequency range (around 0.5–10.0 Hz), such as respirations, heartbeats and gaits, the tunable rheology of the PFM allows for the transduction of acoustic energy into applicable signals at higher frequencies (larger than 30 Hz). This enables an accurate capture and conversion of the acoustic waves into high-fidelity electrical signals.

#### **Motion artefact mitigation**

Motion artefacts can cause fluctuations or distortions in the signals measured by wearable sensors. This leads to inaccurate data, potentially affecting the reliability of measurements for physical signals and the detection of important events due to signal interference<sup>33–35</sup>. Moreover, mitigating motion artefacts often requires complex signal processing algorithms, which can increase computational demands

and power consumption, potentially impacting battery life and overall device performance.

The liquid acoustic sensor was found to mitigate the motion artefacts better than the solid acoustic sensor, and it holds distinct advantages in offering high-quality signals. A comparison was made between the liquid sensor and the solid acoustic sensor as it was attached to the throat. Here we have chosen a capacitive-based acoustic microphone as the solid acoustic sensor, given its widespread use in daily applications. First, we measured the electrical output from both solid and liquid acoustic sensors (Fig. 4e). Due to the air gap between the solid sensor and skin, the calculated results suggested that the liquid acoustic sensor realized a high SNR of 69.1 dB compared with that of the solid acoustic sensor (18.4 dB). Although human biomechanical motions are in the low-frequency range of less than 30 Hz (ref. 32), the modified liquid acoustic sensor enables the removal of low-frequency mechanical signals. In Fig. 4f, the electrical signal of the liquid acoustic sensor with DEG is represented by the red area; the output of the sensor without DEG is depicted by the grey area. Evidently, the red area in this figure exhibits a lower amplitude compared with the grey area, indicating the effective mitigation of low-frequency signals. For comparison purposes, we conducted tests on the solid acoustic sensor along with the presence of motion artefacts caused by movement of the neck and

a simulated noise environment (90 dB). Figure 4g shows that the liquid acoustic sensor exhibits stable performance even in the presence of such interferences. Conversely, the solid acoustic sensor was susceptible to the 90 dB noises and vibrations from the human body. The electrical signals from the liquid sensor and its corresponding acoustic spectrogram are clean and without these interferences (Fig. 4h,i).

Moreover, incorporating a cavity into the liquid sensor negatively impacted its sensing performance. This observation further supports the importance of a conformal interface between the acoustic sensor and human skin for optimal functionality (Supplementary Note 2). To comprehensively demonstrate the liquid acoustic sensor's performance, we created a radar graph to compare its acoustic performance with that of the commercial solid acoustic sensor (Supplementary Fig. 16). The liquid acoustic sensor shows better performance across all the six parameters including SNR, acoustic impedance, conformability, discriminating pressure, detection resolution and accuracy. Moreover, despite the interference of electromagnetic fields emanating from surrounding electronic devices, the voice recordings by the liquid acoustic sensors still maintained high quality (Supplementary Fig. 17). Additionally, the liquid acoustic sensor is insensitive to temperature changes, and can maintain stable performance within the normal human body temperature range (Supplementary Note 3).

#### Wearable voice recognition system

Acoustic sensors and voice recognition technologies have led to a rapid advancement in human—machine interaction and artificial intelligence. To showcase the application of the liquid acoustic sensor, a wearable voice recognition system was further developed to control a wheelchair. It aims to use voice signals to effectively command smart wheelchairs through given prompts and reliable responses with the assistance of machine learning algorithms (Fig. 5a).

The wearable voice recognition system consisted of the liquid acoustic sensor and a customized printed circuit board (Fig. 5b). The printed circuit board was designed to acquire and process the sound-wave-generated electrical signals from the liquid acoustic sensor. It holds three sections. First, an analogue signal pre-processing circuit was used for sound-wave signal acquisition and conditioning. An amplifier was applied to further increase the analogue signals. Next, an analogue-to-digital converter (ADC) was used to collect and convert the analogue electrical signals into digital signals. A machine learning algorithm was applied to recognize the sound signals acquired from the devices to give a command. Then, the control commands were sent to the smart wheelchair by controlling the two motors of the wheelchair to execute the corresponding action of the voice command.

Convolutional neural networks (CNNs) were used in the wearable voice recognition system to increase the recognition accuracy of the command signals. As shown in Fig. 5c, a three-layer CNN was constructed for signal feature extraction and automatic recognition of voice signals. In Fig. 5d, a dataset containing five voice commands is established by repeating each voice command for 720 iterations. The 720 samples of each command were pre-processed by sampling a one-second series to generate training sets. After the model training, a different dataset containing random commands was used to test the model. The temporal progression of the model's accuracy and loss function revealed that the peak recognition accuracy was achieved after 15 training epochs (Fig. 5e). The results showed that our system can achieve the recognition of different voice commands with an accuracy of 99%. Subsequently, to evaluate the sensing and recognizing efficacy of the smart wheelchair, we constructed a confusion matrix to represent the recognition results (Fig. 5f).

To demonstrate the practicality of the wearable voice recognition system, five voice commands were used to control the smart wheelchair: 'go', 'stop', 'left', 'right' and 'back'. Voice commands allow the user to move around independently (Fig. 5g). We tested a smart wheelchair commanded by the wearable voice recognition system. With different

commands, the wearable voice recognition system accurately captured the commands and identified them to control the wheelchair to move around (Fig. 5h). This wearable voice recognition system facilitates the timely control of the wheelchair's movement through voice commands. To further shorten the response time of the voice recognition system, three potential strategies could be adopted, including optimizing signal processing, reducing latency in data transmission and optimizing algorithms. In addition, by attaining higher-quality sensing signals and eliminating motion artefacts, we can reduce the time consumption of signal processing. Consequently, this improvement could also enhance the detection accuracy in the machine learning segment of the system.

#### **Conclusions**

We have reported a self-filtering liquid acoustic sensor for voice recognition. The approach is based on a PFM, which stays magnetized without the presence of external magnetic fields, and has a coercive magnetic field of around 0.1 T and a remanent magnetization of 12.4 A  $\rm m^2\,kg^{-1}$ . We showed that the rheological properties of the PFM can be tuned to both shear thinning and shear thickening through a dynamical chain break–reconnection mechanism and additives. This allows the frequency response range to be tuned to the dynamic acoustic waves of human voices. The resulting liquid acoustic sensor showed an SNR of 69.1 dB and self-filtering capabilities to mitigate motion artefacts. With the assistance of a machine learning algorithm, we constructed a wearable voice recognition system that offered a recognition accuracy of 99%. We also showed that the wearable voice recognition system can be used to control a wheelchair.

The conformability of our liquid acoustic sensor overcomes challenges related to solid acoustic sensors. For example, compared with hydrogels<sup>36,37</sup>, our PFM exhibits lower acoustic impedances and better skin conformability (Supplementary Table 1). The liquid acoustic sensor has potential applications beyond voice recognition, including monitoring and assessing vocal health, detecting changes in voice patterns and identifying potential vocal disorders. For individuals with voice impairments, it could offer an alternative communication method by detecting throat movements and translating them into audible voice or text.

#### Methods

#### Synthesis of permanent fluidic magnets

The NdFeB magnetic nanoparticles (diameter, 200 nm) were specifically fabricated by Nanochemazone. Subsequently, a layer of  $\mathrm{SiO}_2$  was applied to the magnetic nanoparticles through the hydrolysis and polycondensation of tetraethyl orthosilicate (Sigma-Aldrich). The NdFeB magnetic nanoparticles were then mixed with 2–4 wt% sodium alginate or silicone fluids. The volume percentage of the NdFeB magnetic nanoparticles varied from 4 to 28 vol% with carrier fluids. Once thoroughly mixed, the magnetic nanoparticles were subjected to sonication dispersion using an ultrasonic homogenizer (FS-550T) operating at a power of 550 W for 3 h. To modify the PFM, 2–5% DEG (Sigma-Aldrich), polyethylene glycol (Sigma-Aldrich) or fumed silica (Sigma-Aldrich) was added inside before the magnetization procedure. Following the dispersion process, the mixture was magnetized using impulse fields ranging from 0.05 to 2.27 T with an impulse magnetizer (IM-10-30, ASC Scientific).

#### Fabrication of a liquid acoustic sensor

Copper wires were first warped into a helix coil. Then, the PFM was put into the helix coils. After that, a thin layer of polydimethylsiloxane substrate (SYLGARD 184; mixing ratio, 10:1) was coated on the permanent fluidic magnets to seal the device, which was further cured under exposure to UV light.

#### Structure characterization

The morphology of the magnetic powder was characterized by scanning electron microscopy (Zeiss Supra 40VP). The morphology of the

PFM was characterized by a Zeiss Axio Observer Z1 inverted microscope. A superconducting quantum interference device magnetometer (Quantum Design, MPMS3) was used to test the magnetic hysteresis loop. The magnetic flux density mapping on the surface of the PFM was achieved by using the Hall effect sensor (Melexis, MLX90393) mounted on a three-axis motion platform. Transmission electron microscopy images were obtained by a TF20 high-resolution electron microscope (FEI). The temperature variations were captured using a thermal camera (TOPDON, TC001) across a range from 0 to 247 °C.

#### Rheological properties characterization

The storage modulus and loss modulus were measured with a rheometer (AR-2000, TA Instruments). A 20-mm-diameter steel plate was used to hold the sample. The shear rate was applied from 0 to  $100 \, {\rm s}^{-1}$ . In the oscillation experiment, the sweep of stress was applied from 10 to  $10,000 \, {\rm Pa}$ . All the experiments were tested at a fixed temperature of 36 °C.

#### **Electrical output measurement**

The voltage and current signals of the liquid acoustic sensor were measured by a voltage preamplifier (SR560, Stanford) and current preamplifier (SR570, Stanford), respectively. A commercial loudspeaker (R10200, JBL) was used to produce ambient noise. To simulate the voice from human throat, a piezoelectric thin film was used to generate the sound, which was driven by a function generator (AFG1062, Newark) and a power amplifier (PA-151, Labworks) to output the sound wave. Sound waves from 1 Hz to 10 kHz were generated by a Python 3.7 script. The setup is schematically illustrated in Supplementary Fig. 18. A decibel meter (GM1352, Benetech) was used to measure the sound pressure.

#### Design the circuitry for the smart wheelchair

A customized printed circuit board was designed to acquire and process the sound-wave signals generated by the liquid acoustic sensor. First, an analogue signal was amplified using the amplifier (AD620) to acquire the sound-wave signal. Subsequently, the ADC (AD7680) was employed to gather and convert the analogue signals into a digital format. The data from the ADC were then collected by a microcontroller unit (Seeeduino). A CNN algorithm was applied to recognize the sound signals acquired from the devices to control commands. Third, four analogue pins of the microcontroller unit were connected to the joystick input of the wheelchair to send control commands and therefore control the motors of the wheelchair, moving it in different directions. The wheelchair (Culver Mobility) in this work contains brushless motors on each wheel.

#### **Reporting summary**

Further information on research design is available in the Nature Portfolio Reporting Summary linked to this article.

#### Data availability

Source data are provided with this paper. All other data that support the findings of this study are available from the corresponding author on reasonable request.

#### Code availability

Computational simulation code and speech recognition code are available from the corresponding author upon reasonable request.

#### References

- Park, J. et al. Frequency-selective acoustic and haptic smart skin for dual-mode dynamic/static human-machine interface. Sci. Adv. 8, eabj9220 (2022).
- Ma, K. et al. A wave-confining metasphere beamforming acoustic sensor for superior human-machine voice interaction. Sci. Adv. 8, eadc9230 (2022).

- Liu, H. et al. An epidermal sEMG tattoo-like patch as a new human-machine interface for patients with loss of voice. *Microsyst. Nanoena.* 6. 16 (2020).
- Cohen, P. R. & Oviatt, S. L. The role of voice input for human-machine communication. *Proc. Natl. Acad. Sci. USA* 92, 9921–9927 (1995).
- Yang, Q. et al. Mixed-modality speech recognition and interaction using a wearable artificial throat. Nat. Mach. Intell. 5, 169–180 (2023).
- Gong, S. et al. Hierarchically resistive skins as specific and multimetric on-throat wearable biosensors. Nat. Nanotechnol. 18, 889–897 (2023).
- Che, Z. et al. Speaking without vocal folds using a machine-learning-assisted wearable sensing-actuation system. Nat. Commun. 15, 1873 (2024).
- 8. Mathew, L. R., Priya, G. & Gopakumar, K. Piezoelectric throat microphone based voice analysis. In 2021 7th International Conference on Advanced Computing and Communication Systems (ICACCS) 1603–1608 (IEEE, 2021).
- 9. Yan, W. et al. Single fibre enables acoustic fabrics via nanometre-scale vibrations. *Nature* **603**, 616–623 (2022).
- 10. Gao, Y. et al. Hydrogel microphones for stealthy underwater listening. *Nat. Commun.* **7**, 12316 (2016).
- Crut, A., Maioli, P., Del Fatti, N. & Vallée, F. Acoustic vibrations of metal nano-objects: time-domain investigations. *Phys. Rep.* **549**, 1–43 (2015).
- Zhou, Q., Zheng, J., Onishi, S., Crommie, M. F. & Zettl, A. K. Graphene electrostatic microphone and ultrasonic radio. *Proc. Natl. Acad. Sci. USA* 112, 8942–8946 (2015).
- 13. Lee, S. et al. A high-fidelity skin-attachable acoustic sensor for realizing auditory electronic skin. *Adv. Mater.* **34**, 2109545 (2022).
- Lee, S. et al. An ultrathin conformable vibration-responsive electronic skin for quantitative vocal recognition. *Nat. Commun.* 10, 2468 (2019).
- Lin, Z. et al. A personalized acoustic interface for wearable humanmachine interaction. Adv. Funct. Mater. 32, 2109430 (2022).
- Yang, J. et al. Eardrum-inspired active sensors for self-powered cardiovascular system characterization and throat-attached anti-interference voice recognition. Adv. Mater. 27, 1316–1326 (2015).
- Kar, B. & Wallrabe, U. Performance enhancement of an ultrasonic power transfer system through a tightly coupled solid media using a KLM model. *Micromachines* 11, 355 (2020).
- Tang, T. et al. Stretchable polymer composites with ultrahigh piezoelectric performance. *Natl. Sci. Rev.* 10, nwad177 (2023).
- Lavallée, Y. et al. Seismogenic lavas and explosive eruption forecasting. Nature 453, 507–510 (2008).
- Boger, D. V. Demonstration of upper and lower Newtonian fluid behaviour in a pseudoplastic fluid. Nature 265, 126–128 (1977).
- Zhou, Y. et al. Giant magnetoelastic effect in soft systems for bioelectronics. Nat. Mater. 20, 1670–1676 (2021).
- Liu, X. et al. Reconfigurable ferromagnetic liquid droplets. Science 365, 264–267 (2019).
- Mertelj, A., Lisjak, D., Drofenik, M. & Copic, M. Ferromagnetism in suspensions of magnetic platelets in liquid crystal. *Nature* 504, 237–241 (2013).
- 24. Vecchio, D. A., Mahler, S. H., Hammig, M. D. & Kotov, N. A. Structural analysis of nanoscale network materials using graph theory. *ACS Nano* **15**, 12847–12859 (2021).
- 25. Libanori, A., Chen, G., Zhao, X., Zhou, Y. & Chen, J. Smart textiles for personalized healthcare. *Nat. Electron.* **5**, 142–156 (2022).
- 26. Chen, G. et al. Electronic textiles for wearable point-of-care systems. *Chem. Rev.* **122**, 3259–3291 (2022).
- Chen, L., Huang, S., Ras, R. H. A. & Tian, X. Omniphobic liquid-like surfaces. Nat. Rev. Chem. 7, 123–137 (2023).

- Tang, X., Shen, H., Zhao, S., Li, N. & Liu, J. Flexible brain-computer interfaces. Nat. Electron. 6, 109–118 (2023).
- Koo, J. H. et al. A vacuum-deposited polymer dielectric for wafer-scale stretchable electronics. Nat. Electron. 6, 137–145 (2023).
- 30. Jiang, Y. et al. A universal interface for plug-and-play assembly of stretchable devices. *Nature* **614**, 456–462 (2023).
- 31. Yan, Z. et al. Highly stretchable van der Waals thin films for adaptable and breathable electronic membranes. Science **375**, 852–859 (2022).
- Park, B. et al. Cuticular pad-inspired selective frequency damper for nearly dynamic noise-free bioelectronics. Science 376, 624–629 (2022).
- Zhao, Y. et al. Ultra-conformal skin electrodes with synergistically enhanced conductivity for long-time and low-motion artifact epidermal electrophysiology. Nat. Commun. 12, 4880 (2021).
- Ershad, F. et al. Ultra-conformal drawn-on-skin electronics for multifunctional motion artifact-free sensing and point-of-care treatment. *Nat. Commun.* 11, 3823 (2020).
- Yin, J., Wang, S., Tat, T. & Chen, J. Motion artifact management in soft bioelectronics. Nat. Rev. Bioeng. 2, 541–558 (2024).
- Yang, C. & Suo, Z. Hydrogel ionotronics. *Nat. Rev. Mater.* 3, 125–142 (2018).
- Keplinger, C. et al. Stretchable, transparent, ionic conductors. Science 341, 984–987 (2013).

#### **Acknowledgements**

We acknowledge the Henry Samueli School of Engineering & Applied Science and the Department of Bioengineering at the University of California, Los Angeles, for their startup support. J.C. acknowledges the Vernroy Makoto Watanabe Excellence in Research Award at the UCLA Samueli School of Engineering, the Office of Naval Research Young Investigator Award (award ID N00014-24-1-2065), National Science Foundation Grant (award ID 2425858), National Institutes of Health Grant (award ID R01 CA287326), the American Heart Association Innovative Project Award (award ID 23IPA1054908), the American Heart Association Transformational Project Award (award ID 23TPA1141360), the American Heart Association's Second Century Early Faculty Independence Award (award ID 23SCEFIA1157587), the Brain & Behavior Research Foundation Young Investigator Grant (grant

no. 30944) and the NIH National Center for Advancing Translational Science UCLA CTSI (grant no. KL2TR001882).

#### **Author contributions**

J.C. guided the whole research project. X.Z., Y.Z. and J.C. conceived the idea, designed the experiment, analysed the data, drew the figures and wrote the manuscript. A.L., J.X., S.K., E.H., L.R., J.L., J.H. and P.K. assisted in device fabrication and testing. All authors read the paper, agreed to its content and approved the submission.

#### **Competing interests**

A US patent 63/596,815 related to this work has been filed by the University of California, Los Angeles.

#### **Additional information**

**Supplementary information** The online version contains supplementary material available at https://doi.org/10.1038/s41928-024-01196-y.

**Correspondence and requests for materials** should be addressed to lun Chen.

**Peer review information** *Nature Electronics* thanks Sang-Woo Kim and Li Tan for their contribution to the peer review of this work.

**Reprints and permissions information** is available at www.nature.com/reprints.

**Publisher's note** Springer Nature remains neutral with regard to jurisdictional claims in published maps and institutional affiliations.

Springer Nature or its licensor (e.g. a society or other partner) holds exclusive rights to this article under a publishing agreement with the author(s) or other rightsholder(s); author self-archiving of the accepted manuscript version of this article is solely governed by the terms of such publishing agreement and applicable law.

@ The Author(s), under exclusive licence to Springer Nature Limited 2024

# nature portfolio

Corresponding author(s):	Jun Chen
Last updated by author(s):	Apr 5, 2024

## **Reporting Summary**

Nature Portfolio wishes to improve the reproducibility of the work that we publish. This form provides structure for consistency and transparency in reporting. For further information on Nature Portfolio policies, see our <u>Editorial Policies</u> and the <u>Editorial Policy Checklist</u>.

<b>~</b> .			
<b>\</b> †	at.	ıctı	

For	all statistical analyses, confirm that the following items are present in the figure legend, table legend, main text, or Met	nods section.
n/a	Confirmed	
	The exact sample size ( $n$ ) for each experimental group/condition, given as a discrete number and unit of measurer	nent
	A statement on whether measurements were taken from distinct samples or whether the same sample was measurements	ured repeatedly
	The statistical test(s) used AND whether they are one- or two-sided Only common tests should be described solely by name; describe more complex techniques in the Methods section.	
	A description of all covariates tested	
	A description of any assumptions or corrections, such as tests of normality and adjustment for multiple compariso	ns
	A full description of the statistical parameters including central tendency (e.g. means) or other basic estimates (e.g. AND variation (e.g. standard deviation) or associated estimates of uncertainty (e.g. confidence intervals)	;. regression coefficient)
$\boxtimes$	For null hypothesis testing, the test statistic (e.g. <i>F</i> , <i>t</i> , <i>r</i> ) with confidence intervals, effect sizes, degrees of freedom <i>Give P values as exact values whenever suitable.</i>	and P value noted
$\boxtimes$	For Bayesian analysis, information on the choice of priors and Markov chain Monte Carlo settings	
$\times$	For hierarchical and complex designs, identification of the appropriate level for tests and full reporting of outcome	·s
$\boxtimes$	Estimates of effect sizes (e.g. Cohen's $d$ , Pearson's $r$ ), indicating how they were calculated	
	Our web collection on statistics for biologists contains articles on many of the points above.	

#### Software and code

Policy information about availability of computer code

Data collection

Data collection was performed using a Zeiss Axio Observer Z1 inverted fluorescence microscope and Leica SP8-STED/FLIM/FCS confocal microscope for fluorescence imaging; magnetic particle size distribution was determined by ZEISS Supra 40VP and TF20 high-resolution electron microscopy; the electrical signal were recored by LabVIEW 2019; the magnetic hysteresis loops were measured by a SQUID magnetometer Quantum Design, MPMS 3. The magnetic flux density was measured with MLX 90393 Melexis.

Data analysis

Data analysis was performed by free or commercial software platforms, including ImageJ 1.53t. Origin 2018 was used to generate bar charts or box charts and perform statistical analysis. Matlab R2022b was used for the Monte Carlo simulation of the oriented and ramified nanomagnet network.

For manuscripts utilizing custom algorithms or software that are central to the research but not yet described in published literature, software must be made available to editors and reviewers. We strongly encourage code deposition in a community repository (e.g. GitHub). See the Nature Portfolio guidelines for submitting code & software for further information.

#### Data

Policy information about availability of data

All manuscripts must include a data availability statement. This statement should provide the following information, where applicable:

- Accession codes, unique identifiers, or web links for publicly available datasets
- A description of any restrictions on data availability
- For clinical datasets or third party data, please ensure that the statement adheres to our policy

The authors declare that all data supporting the findings of this study are available within the paper, source data, and supplementary information files.

#### Human research participants

Policy information about studies involving human research participants and Sex and Gender in Research.

Reporting on sex and gender

3 male participants were recruited for the experiment to test device performance. Gender and other biographical information were irrelevant for the human study conducted in our experiment.

Population characteristics

The human participants in this study are students at University of California, Los Angeles with the age from 20 - 30 years old. Population characteristics are not relevant to the experiment or the results of this study.

Recruitment

Participants were recruited from the Department of Bioengineering at University of California, Los Angeles.

Ethics oversight

The sensor was used on human subjects in compliance with all the ethical regulations under a protocol (ID: 20-001882) that was approved by the Institutional Review Board (IRB) at University of California, Los Angeles. All participating subjects were affiliated with the University of California, Los Angeles, and were provided informed consent before participation in the study.

Ecological, evolutionary & environmental sciences

Note that full information on the approval of the study protocol must also be provided in the manuscript.

## Field-specific reporting

Please select the one below that is the best fit for y	your research. If you are not sure,	read the appropriate sections	before making your selection.

For a reference copy of the document with all sections, see <a href="mailto:nature.com/documents/nr-reporting-summary-flat.pdf">nature.com/documents/nr-reporting-summary-flat.pdf</a>

Behavioural & social sciences

## Life sciences study design

All studies must disclose on these points even when the disclosure is negative.

Sample size

X Life sciences

A minimum of three independent experiments were carried out for all studies. The sample size necessary to detect a significant effect was estimated by using data from pilot studies. Statistical analysis was performed using Origin 2018 software. A p-value < 0.05 was considered significant.

Data exclusions

No data exclusion in this research

Replication

In all experiments, either replicate or triplicate of samples were processed in parallel. All experiments were performed independently 3 times or more and consistent results were evident across independent experiments.

Randomization

For our experiments, cells isolated from the same batch were used in a given experiment and cells were randomly chosen for the control or experimental groups. Experiments were also performed with different batches of cells to confirm the findings.

Blinding

All data were acquired and analyzed by softwares with objective standard, so blinding is not relevant to the data analysis.

## Reporting for specific materials, systems and methods

We require information from authors about some types of materials, experimental systems and methods used in many studies. Here, indicate whether each material, system or method listed is relevant to your study. If you are not sure if a list item applies to your research, read the appropriate section before selecting a response.

	uti ra portto
ē	2.
	_
	DOCTION OF

S	
5	
3	
٠.	
`	

Materials & experimental systems	Methods
n/a Involved in the study	n/a Involved in the study
Antibodies	ChIP-seq
Eukaryotic cell lines	Flow cytometry
Palaeontology and archaeology	MRI-based neuroimaging
Animals and other organisms	·
Clinical data	
Dual use research of concern	